Temperature-Dependent Sound Absorption Characteristics of Perforated Porous Metamaterials

Xiaozhen Li and Xiaobing Cai*

State Key Laboratory for Strength and Vibration of Mechanical Structures, School of Aerospace Engineering, Xi'an Jiaotong University, Xi'an 710049, China

Abstract: Recent studies have demonstrated that sound absorption performance can be improved by constructing macroscopic perforations on a porous material matrix. In this paper, the temperature-dependent sound absorption characteristics of three different perforated porous materials (PPMs) with cylindrical (C-PPM), normal conical (NC-PPM) and reverse conical (RC-PPM) perforations are comparatively studied. We used a double porosity theoretical model to study the high-temperature sound absorption of these PPMs and validated it by numerical simulations. The sound absorption mechanism and temperature effect are revealed by the numerical distributions of sound pressure, sound energy dissipation density and sound intensity flow. The results show that the PPMs exhibit better sound absorption than porous material matrix (PMM), especially at low frequencies. This is attributed to the pressure diffusion effect of PPMs, and this effect is enhanced by high temperatures. Furthermore, the three PPMs have sound absorption peaks in different frequency ranges, but high temperatures delay their appearance. Finally, we discussed the effects of perforated shape, perforated size and material properties on sound absorption and identified their optimal values.

Keywords: Porous material, Perforation, Sound absorption, Temperature effect.

1. INTRODUCTION

In recent decades, the rapid development of aerospace and automotive industries has brought increased attention to noise reduction in high-temperature environments. As a typical case, the complex and intense noise from extreme environments like engine combustion chambers can easily penetrate protective enclosures, thereby affecting the operation of equipment and instruments [1]. Therefore, it is crucial to design and develop acoustic materials or structures capable of absorbing sound and reducing noise in high-temperature environments. Historically, porous materials, renowned for their excellent sound-absorbing capability and high-temperature resistance [2], have been extensively employed in the field of sound absorption and noise reduction at high temperatures. Common porous materials such as metal foam or fibers [3-6] and ceramic fibers [7-10], have proven to be reliable sound-absorbing materials for practical applications due to their lightweight, inexpensive and good sound absorption.

However, these conventional sound-absorbing materials perform well in the high-frequency range but are less effective in the low-frequency range. To address this issue, various artificially designed sound-absorbing metamaterials or structures have been developed. For example, acoustic metamaterials with hierarchical structures [11-17], acoustic metamaterials with micro-perforated plate sandwiches [15, 18-20], acoustic metamaterials attached with resonators [21-26], and acoustic metamaterials designed and optimized by deep learning [27, 28]. Although these artificially designed acoustic metamaterials have excellent low-frequency and broadband sound absorption, most of the current research has been conducted at room temperature, with fewer studies involving high temperatures. However, recent studies have shown that multi-scale porous metamaterials can significantly enhance low-frequency sound absorption at high temperatures. That is, the sound absorption is improved by artificially constructing macroscopic perforations or slits on a porous material matrix. For example, Liu *et al*. [29] studied the high-temperature sound absorption of cylindrical perforated porous materials at 500 °C. Zhang *et al*. [30, 31] studied the high-temperature sound absorption of labyrinthine perforated porous materials at 500 °C and helical perforated porous materials at 600 °C, respectively. The reported research has shown that the constructed macroscopic perforations can greatly improve the low-frequency sound absorption than non-perforated porous material matrix. Significantly, the geometric parameters of macroscopic perforations have an important impact on the improvement of sound absorption. Different geometric parameters correspond to improved sound absorption in different frequency ranges. Therefore, in order to achieve the best sound absorption for given application frequency ranges, it is essential to precisely adjust the geometric shape and size of macroscopic perforations.

In this paper, we comparatively studied the high-temperature sound absorption characteristics of three

*Address correspondence to this author at State Key Laboratory for Strength and Vibration of Mechanical Structures, School of Aerospace Engineering, Xi'an Jiaotong University, Xi'an 710049, China;
E-mail: caixiaobing@xjtu.edu.cn

perforated porous materials (PPMs), including cylindrical-perforated porous material (C-PPM), normal conical-perforated porous material (NC-PPM) and reverse conical-perforated porous material (RC-PPM). These PPMs are constructed by perforating macroscopic holes on porous material matrix (PMM) with micropore sizes under sub-millimeters. We used the double porosity theoretical model considering temperature effects to characterize the high-temperature sound absorption characteristics and then validated it by numerical simulations. The high-temperature effect is discussed by analyzing the sound absorption coefficient and surface impedance at different temperatures. Furthermore, based on the numerical distributions of sound pressure, energy dissipation density and sound intensity flow, the sound absorption mechanism is further revealed. Finally, we studied the influence of perforated shapes and sizes as well as material properties on sound absorption, and explored their optimal values for improving sound absorption.

2. THEORETICAL MODEL

As shown in Figure **1**, three PPM plates are presented, whose geometrical shapes of perforations are cylindrical, normal conical and reverse conical

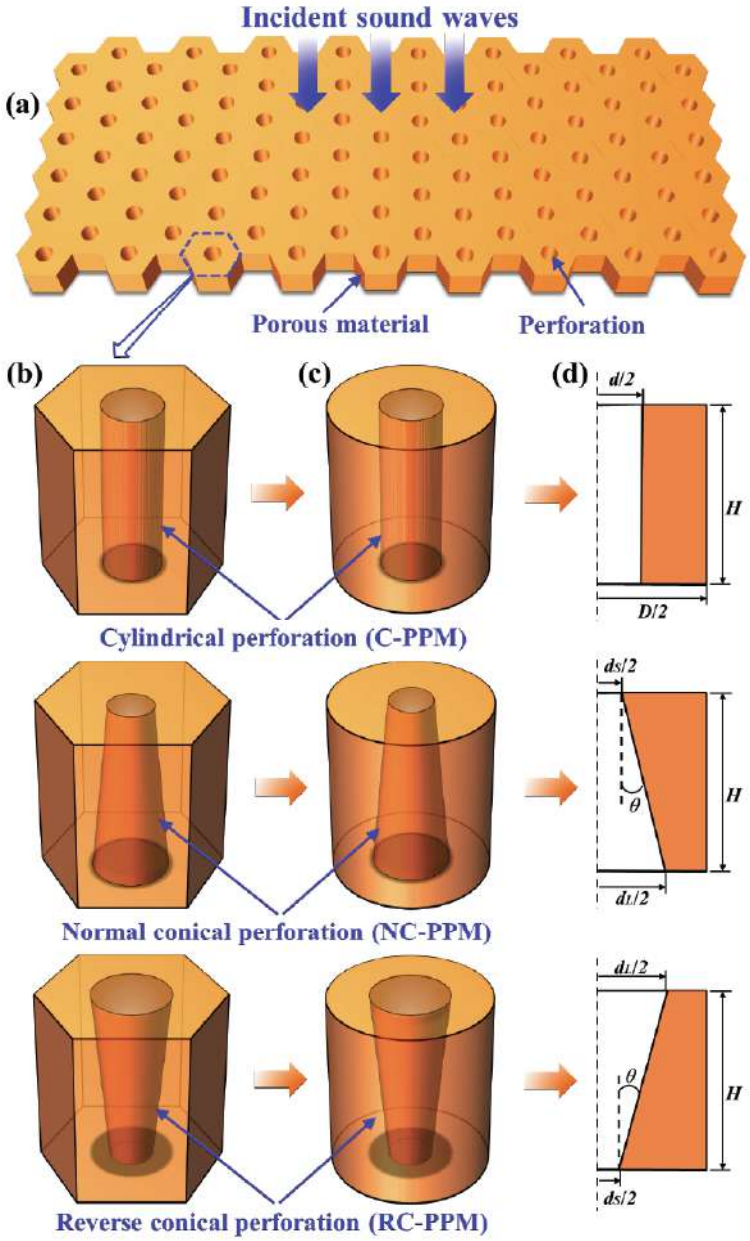

Figure 1: (**a**) Perforated porous material plates with cylindrical perforation, normal and reverse conical perforation; (**b**) Hexagonal unit; (**c**) Equivalent cylindrical unit; (**d**) Axisymmetric cross sections showing the main geometric parameters.

perforations. The three PPM plates are exposed to high temperatures (20 ~ 500 ℃). Their upper surfaces are subjected to downward incident sound waves while their lower surfaces are terminated by an acoustic hard boundary in Figure **1a**. In this paper, a hexagonal unit is extracted to representatively study the sound absorption of the periodic PPM plates in Figure **1b**. Then, a cylindrical unit with the same volume is used to be approximately equivalent to the hexagonal unit in Figure **1c**. Correspondingly, the axisymmetric cross sections are shown in Figure **1d**, describing the main geometric parameters: the height and diameter of one unit are H and D; the diameter of cylindrical perforation is d; the upper diameter of normal conical perforation is d_S and the lower diameter is d_L; the upper diameter of reverse conical perforation is d_L and the lower diameter is d_S; and the gradient angles of two conical perforations are $\pm\theta$ (normal conical perforation: $+\theta$, reverse conical perforation: $-\theta$) that related to d_S and d_L. To comparatively study the sound absorption of three PPM plates, their perforation volumes are set to be the same. Overall, the above equivalent method can greatly simplify the calculations and maintain the evaluation of sound absorption of the whole periodic porous material.

2.1. The Model Considering Cylindrical Perforation

Since the C-PPM consists of PMM and cylindrical perforation with the perforated porosity of $\phi_p = d^2/D^2$, the double porosity theory is considered. The C-PPM can be equated to a new homogeneous porous material with the same volume. Therefore, the equivalent acoustic mass density ρ_{eq} and bulk modulus K_{eq} is expressed as [32]

$$\rho_{eq} = \left(\frac{1}{\rho_p} + \frac{\left(1-\phi_p\right)}{\rho_m} \right)^{-1} \tag{1}$$

$$K_{eq} = \left(\frac{1}{K_p} + \frac{\left(1-\phi_p\right) F_d\left(\omega\right)}{K_m} \right)^{-1} \tag{2}$$

where ρ_m and K_m are the acoustic mass density and bulk modulus of PMM; ρ_p and K_p are the mass density and bulk modulus of cylindrical perforation; $F_d(\omega)$ is the ratio of average sound pressure in porous material to that in cylindrical perforation.

On the one hand, the mass density ρ_m and bulk modulus K_m of PMM are defined by the Johnson-Champoux-Allard (JCA) model as [33, 34]

$$\rho_m = \frac{\rho\alpha_{\infty m}}{\phi_m}\left(1 + \frac{\phi_m\sigma_m}{j\omega\rho\alpha_{\infty m}}\cdot\sqrt{1 + j\frac{4\omega\eta\rho\alpha_{\infty m}^2}{\phi_m^2\sigma_m^2\Lambda_m^{'2}}}\right) \tag{3}$$

$$K_m = \frac{\gamma P_0}{\phi_m}\left(\gamma - \frac{\gamma-1}{1 - j\dfrac{8\kappa}{\omega\rho C_p\Lambda_m^{'2}}\cdot\sqrt{1 + j\dfrac{\omega\rho C_p\Lambda_m^{'2}}{16\kappa}}}\right)^{-1} \tag{4}$$

where $j=\sqrt{-1}$. is an imaginary unit; $\omega = 2\pi f$ is an angular frequency; P_0 is a standard atmospheric pressure; ρ, η, C_p κ, γ, are the density, dynamic viscosity, specific heat capacity, thermal conductivity, specific heat ratio of air, respectively; and ϕ_m, $\alpha_{\infty m}$, σ_m, Λ_m, $\Lambda_m^{'}$ are the porosity, tortuosity, static flow resistivity, viscous characteristic length, thermal characteristic length of porous material, respectively.

On the other hand, the acoustic mass density ρ_p and bulk modulus K_p of cylindrical perforation are written as [29]

$$\rho_p = \frac{\rho}{\phi_p}\left(1 - \frac{2}{\mu\sqrt{-j}}\cdot\frac{J_1\left(\mu\sqrt{-j}\right)}{J_0\left(\mu\sqrt{-j}\right)}\right)^{-1} \tag{5}$$

$$K_p = \frac{\gamma P_0}{\phi_p}\left(1 + \frac{2\left(\gamma-1\right)}{\mu\sqrt{-jP_r}}\frac{J_1\left(\mu\sqrt{-jP_r}\right)}{J_0\left(\mu\sqrt{-jP_r}\right)}\right)^{-1} \tag{6}$$

where $\mu = \dfrac{d\sqrt{\omega\rho}}{2\sqrt{\eta}}$; $P_r = \dfrac{\eta C_p}{\kappa}$ is the Prandtl number; and $J_0(\cdot)$ and $J_1(\cdot)$ are the zero-order and first-order Bessel functions, respectively.

Furthermore, the function $F_d(\omega)$ in Eq.2 is defined as [32, 35]

$$F_d\left(\omega\right) = \left(1 - j\frac{\omega}{\omega_d}\frac{D\left(\omega\right)}{D\left(0\right)}\right) \tag{7}$$

where $D(\omega)$ is related to thermal permeability and is used to describe thermal effects; and $D(0)$ is a geometric parameter comparable to static thermal permeability.

$D(\omega)$ is written as [32, 35]

$$D\left(\omega\right) = \frac{D\left(0\right)}{j\dfrac{\omega}{\omega_d} + \left(1 + j\dfrac{M_d\omega}{2\omega_d}\right)^{\frac{1}{2}}} \tag{8}$$

$D(0)$ is written as [29]

$$D\left(0\right)=\frac{D^2}{16}\left(\ln\left(\frac{1}{\phi_p}\right)-\frac{3}{2}+2\phi_p-\frac{\phi_p^{\ 2}}{2}\right) \tag{9}$$

where

$$\omega_d=\frac{\left(1-\phi_p\right)P_0}{D\left(0\right)\phi_m\sigma_m} \tag{10}$$

is defined as the characteristic frequency of sound pressure diffusion effects;

and

$$M_d=\frac{8D\left(0\right)}{\left(1-\phi_p\right)\Lambda_d^{\ 2}} \tag{11}$$

is a form parameter with

$$\Lambda_d=2\frac{\Omega_{mp}}{\partial\Omega_{mp}} \tag{12}$$

where Ω_{mp} is the volume of perforated porous material and $\partial\Omega_{mp}$ is the interface area of porous material in contact with air. For cylindrical sample and perforation, the two are written as

$$\Omega_{mp}=\left(\frac{\pi D^2}{4}-\frac{\pi d^2}{4}\right)H \tag{13}$$

$$\partial\Omega_{mp}=\left(\frac{\pi D^2}{4}-\frac{\pi d^2}{4}\right)+\pi dH \tag{14}$$

Based on the above analytical steps, the acoustic characteristic impedance Z_{eq} and the acoustic wavenumber k_{eq} of PPMs are defined as

$$Z_{eq}=\sqrt{\rho_{eq}K_{eq}} \tag{15}$$

$$k_{eq}=\omega\sqrt{\frac{\rho_{eq}}{K_{eq}}} \tag{16}$$

Then, surface characteristic impedance Z_s is defined as

$$Z_s=-jZ_{eq}\cot\left(k_{eq}H\right) \tag{17}$$

The sound reflection coefficient r is defined as

$$r=\frac{Z_s-Z_0}{Z_s+Z_0} \tag{18}$$

where $Z_0=\rho c$ is the characteristic impedance of air, with ρ being the mass density and c being the sound speed of air.

The relationship between the sound reflection coefficient r and the normalized surface impedance Z_s/Z_0 of normal incident sound waves is expressed by

$$\frac{Z_s}{Z_0}=\frac{1+r}{1-r} \tag{19}$$

The relationship between sound absorption coefficient α and reflection coefficient r is defined as

$$\alpha=1-\left|r\right|^2 \tag{20}$$

and α can also be expressed in terms of the surface impedance Z_s as follows:

$$\alpha=\frac{4\,\mathrm{Re}\left(Z_s\right)/Z_0}{\left[1+\mathrm{Re}\left(Z_s\right)/Z_0\right]^2+\left[\mathrm{Im}\left(Z_s\right)/Z_0\right]^2} \tag{21}$$

where $\mathrm{Re}(Z_s)$ and $\mathrm{Im}(Z_s)$ are the real and imaginary parts of Z_s, respectively.

2.2. The Model Considering Conical Perforation

Since the conically perforated porous material (NC-PPM or RC-PPM) consists of PMM and conical perforation (normal or reverse conical perforation), and the conical perforation can be regarded as a superimposed combination of cylindrical perforations with different perforation diameters, thus the double porosity theory can still be used. Figure **2** shows a schematic of conical perforation equivalent to N-layer cylindrical perforation. For simplicity, the conical perforation is divided into N layers with the same thickness $h = H/N$.

For the i-th layer equivalent cylindrical perforations, its diameter is written as

$$d_i=\frac{\left(i-\frac{1}{2}\right)\left(d_L-d_S\right)}{N}+d_S \tag{22}$$

and its volume is written as

$$\Omega_{mp\_i}=\frac{\left(D^2-d_i^{\ 2}\right)\pi h}{4} \tag{23}$$

For NC-PPM, the interfacial area between porous material and air is written as

$$\partial\Omega_{mp\_i} = \frac{\left(D^2 - d_i^2\right)\pi}{4} + \pi d_i h\ , \quad i = 1 \tag{24}$$

$$\partial\Omega_{mp\_i} = \frac{\left(d_i^2 - d_{i-1}^2\right)\pi}{4} + \pi d_i h\ , \quad i = 1,\ 2,\ \ldots N \tag{25}$$

For RC-PPM, the interfacial area between porous material and air is written as

$$\partial\Omega_{mp\_i} = \frac{\left(d_{i+1}^2 - d_i^2\right)\pi}{4} + \pi d_i h\ , \quad i = 1,\ 2,\ \ldots N-1 \tag{26}$$

$$\partial\Omega_{mp\_i} = \frac{\left(D^2 - d_i^2\right)\pi}{4} + \pi d_i h\ , \quad i = N \tag{27}$$

For the *i*-th layer C-PPM, the new equivalent mass density ρ_{eq_i} and bulk modulus K_{eq_i} are written as [36-38]

$$\rho_{eq\_i} = \left(\frac{1}{\rho_{p\_i}} + \frac{\left(1-\phi_{p\_i}\right)}{\rho_m}\right)^{-1} \tag{28}$$

$$K_{eq\_i} = \left[\frac{1}{K_{p\_i}} + \frac{\left(1-\phi_{p\_i}\right)F_{d\_i}\left(\omega\right)}{K_m}\right]^{-1} \tag{29}$$

where the acoustic mass density ρ_m and bulk modulus K_m of PMM are still expressed by Eq. 3 and Eq. 4; while the acoustic mass density ρ_{p_i} and bulk modulus K_{p_i} of *i*-th layer perforation are written as

$$\rho_{p\_i} = \frac{\rho}{\phi_{p\_i}}\left(1 - \frac{2}{\mu_i\sqrt{-j}}\frac{J_1\left(\mu_i\sqrt{-j}\right)}{J_0\left(\mu_i\sqrt{-j}\right)}\right)^{-1} \tag{30}$$

$$K_{p\_i} = \frac{\gamma P_0}{\phi_{p\_i}}\left(1 + \frac{2\left(\gamma-1\right)}{\mu_i\sqrt{-jP_r}}\cdot\frac{J_1\left(\mu_i\sqrt{-jP_r}\right)}{J_0\left(\mu_i\sqrt{-jP_r}\right)}\right)^{-1} \tag{31}$$

and the function $F_d(\omega)$ in Eq.7 is rewritten as

$$F_{d\_i}\left(\omega\right) = 1 + \frac{1}{j\dfrac{\omega_{d\_i}\phi_m K_m}{\omega P_0}\cdot\left(1 + j\dfrac{M_{d\_i}}{2}\dfrac{\omega P_0}{\omega_{d\_i}\phi_m K_m}\right)^{1/2} - 1} \tag{32}$$

Then, the acoustic characteristic impedance Z_{dp_i} and wavenumber k_{dp_i} are written as

$$Z_{eq\_i} = \sqrt{\rho_{eq\_i}K_{eq\_i}} \tag{33}$$

$$k_{eq\_i} = \omega\sqrt{\frac{\rho_{eq\_i}}{K_{eq\_i}}} \tag{34}$$

To obtain the acoustic characteristics of the whole multilayer system, the relationship of acoustic parameters between adjacent layers can be established by the transfer matrix method [36]

$$\begin{pmatrix} p_i \\ v_i \end{pmatrix} = \mathbf{T}_i \begin{pmatrix} p_{i-1} \\ v_{i-1} \end{pmatrix} \tag{35}$$

$$\mathbf{T}_i = \begin{bmatrix} T_{i(11)} & T_{i(12)} \\ T_{i(21)} & T_{i(22)} \end{bmatrix} = \begin{bmatrix} \cos\left(k_{eq\_i}\cdot h\right) & jZ_{eq\_i}\sin\left(k_{eq\_i}\cdot h\right) \\ j\dfrac{1}{Z_{eq\_i}}\sin\left(k_{eq\_i}\cdot h\right) & \cos\left(k_{eq\_i}\cdot h\right) \end{bmatrix} \tag{36}$$

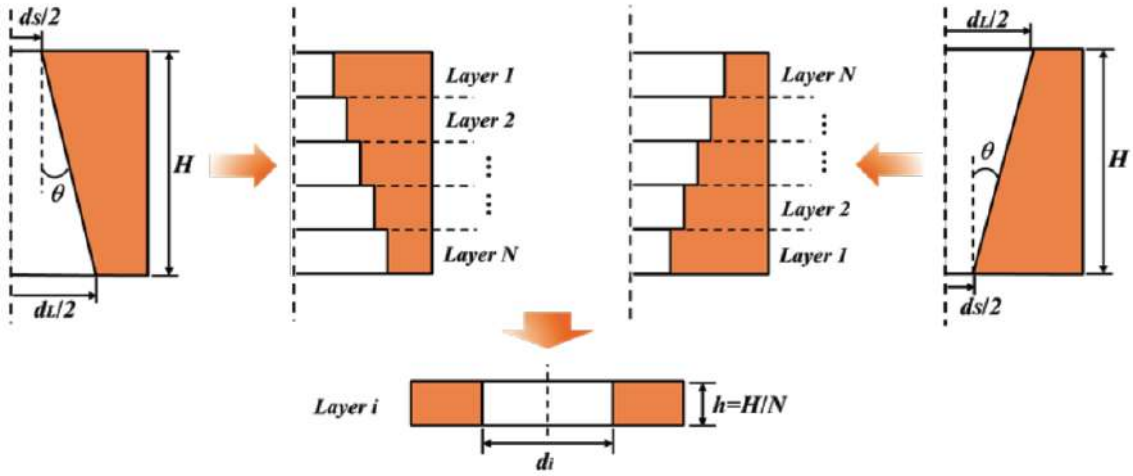

Figure 2: Schematic of conical perforation equivalent to N-layer cylindrical perforation.

Table 1: The Values of the Fitting Parameters A_n and B_n [29]

A_n	Values (W/m/K^{n+1})	B_n	Values (J/kg/K^{n+1})
A_0	−0.00227583562	B_0	1047.63657
A_1	1.15480022×10^{-4}	B_1	−0.372589265
A_2	-7.90252856×10^{-8}	B_2	9.45304214×10^{-4}
A_3	4.11702505×10^{-11}	B_3	-6.02409443×10^{-7}
A_4	$-7.43864331\times10^{-15}$	B_4	1.2858961×10^{-10}

where $\mathbf{T}_i$ is the transfer matrix of i-th layer; p_{i-1}, v_{i-1}, p_i, v_i are the sound pressure and particle vibration velocity of adjacent layers.

Then, the transfer matrix of the whole multilayer system is written as

$$\mathbf{T}=\begin{bmatrix} T_{(11)} & T_{(12)} \\ T_{(21)} & T_{(22)} \end{bmatrix}=\prod_{i=1}^{N}\mathbf{T}_i=\mathbf{T}_1\mathbf{T}_2\mathbf{T}_3\cdots\mathbf{T}_N \tag{37}$$

The surface impedance Z_s of the whole multilayer system is expressed by

$$Z_s=\frac{T_{(11)}}{T_{(21)}} \tag{38}$$

The sound reflection coefficient r is defined as [39]

$$r=\frac{T_{(11)}-T_{(21)}Z_0}{T_{(11)}+T_{(21)}Z_0} \tag{39}$$

Finally, according to Eq. 20 or Eq. 21, the sound absorption coefficient α of the whole multilayer system can be obtained.

2.3. Temperature-Dependent Acoustic Parameters

As is well known, the temperature effect has an important impact on sound absorption. Temperature can change the physical parameters of air, such as mass density ρ, sound speed c, and dynamic viscosity η, etc. The temperature-dependent density ρ, sound speed c, and dynamic viscosity η of air are expressed as [18]

$$\rho=\frac{P_0M}{RT} \tag{40}$$

$$c=\sqrt{\frac{\gamma RT}{M}} \tag{41}$$

$$\eta=\eta_0\left(\frac{T}{T_0}\right)^{\frac{3}{2}}\left(\frac{C+T_0}{C+T}\right) \tag{42}$$

where P_0 = 101330 Pa; T_0 and T are the room and given temperature in Kelvin, respectively; M = 0.02897 kg/mol, R = 8.314 J/mol/K, γ = 1.4 are the molar mass, molar gas constant, specific heat ratio of air, respectively; η_0 = 1.827 × 10^{-5} Pa·s is the dynamic viscosity at T_0, and C = 120 K.

Furthermore, temperature change also alters the specific heat capacity C_p and thermal conductivity κ of air [29, 40]

$$C_p=A_0+A_1T+A_2T^2+A_3T^3+A_4T^4 \tag{43}$$

$$\kappa=B_0+B_1T+B_2T^2+B_3T^3+B_4T^4 \tag{44}$$

where the values of fitting parameters A_n and B_n are listed in Table **1**.

In addition to the above air physical parameters, temperature also affects the static flow resistivity σ_m of porous materials [41, 42]

$$\sigma_m=\sigma_0\cdot\left(\frac{T}{T_0}\right)^{0.6} \tag{45}$$

where σ_0 is the static flow resistivity at T_0.

3. FINITE ELEMENT SIMULATION

3.1. Numerical Model

In COMSOL Multiphysics, the Pressure Acoustic Module is used for numerical modeling and simulation. For simplicity, a two-axisymmetric model is used to simulate four sound-absorbing materials, as shown in Figure **3**. The geometric sizes of four models: H = 60 mm; D = 60 mm; d = 24 mm; θ = ±10° (normal conical perforation: θ = +10°, reverse conical perforation: θ = −10°). Furthermore, due to three PPMs having the same perforated volume and the two conical perforations being transposed to each other, d_S and d_L can be determined. In these models, the brown region is a porous material made of metal fibers and set as a poroacoustic domain using the JCA model with five

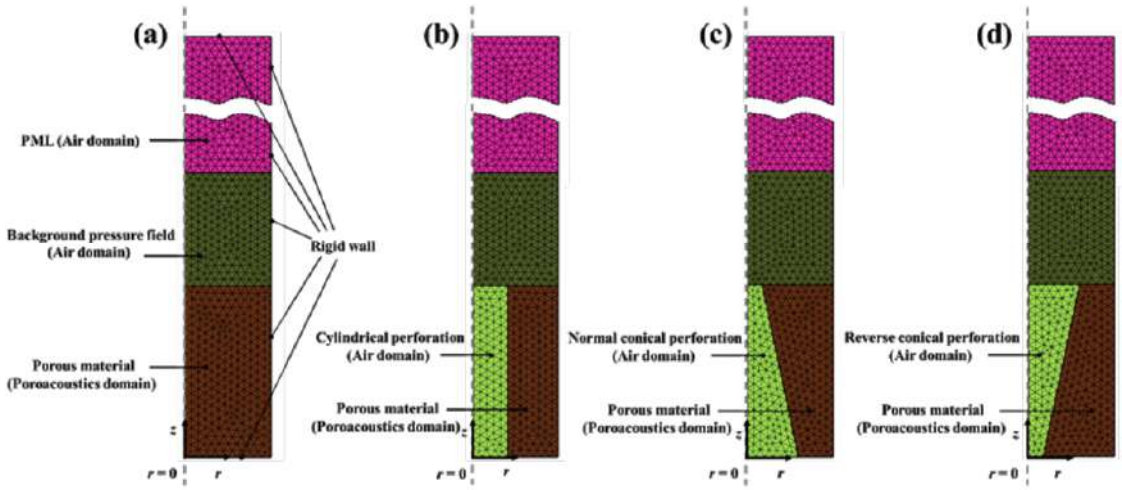

Figure 3: Two-dimensional axisymmetric finite element models: (**a**) PMM without any perforation; (**b**) C-PPM with cylindrical perforation; (**c**) C-PPM with normal conical perforation; (**d**) C-PPM with reverse conical perforation.

parameters at 20 ℃: σ_m = 489336 N·s/m^4; ϕ_m = 0.9; $\alpha_{\infty m}$ = 1.05; Λ_m = 19.7 μm; $\Lambda_m^{'}$ = 36 μm [30]. The dark green region is a background pressure field that is used to provide incident sound waves, and this region is also set as an air domain. The red region is a perfectly matched layer (PML) and the yellow region is a perforation, both of which are set as air domains. Furthermore, the outer boundaries of these models are set as acoustic hard boundaries.

Furthermore, in COMSOL Multiphysics, all physical parameters and expressions are defined. An incident sound wave with an amplitude of 1.0 Pa is defined to propagate along the -z direction. In numerical simulations, the surface characteristic impedance Z_s is calculated by

$$Z_s = \frac{\langle p \rangle_s}{\langle v_z \rangle_s} \tag{46}$$

where $\langle p \rangle_s$ and $\langle v_z \rangle_s$ are the average sound pressure and the average particle velocity on the upper surface of porous materials and perforations, respectively. Finally, at different temperatures ($T = t$ + 273.15 K, t = 20 ℃, 100 ℃, 300 ℃, 500 ℃), the sound absorption coefficients are numerically extracted within the frequency of 3000 Hz.

3.2. Numerical Validation

The comparison results between theoretical predictions and numerical simulations of acoustic characteristics for four sound-absorbing materials at different temperatures are shown in Figure **4**. As shown in Figure **4a**, the theoretical predictions and numerical simulations are in good agreement for PMM at all temperatures. The sound absorption coefficients decrease with temperature, which indicates that high temperatures would weaken sound absorption performance. According to the normalized surface impedance curves, the real part of surface impedance increases with temperature and moves away from the value 1, whereas the imaginary part of surface impedance decreases with temperature and moves away from the value 0. This suggests that the surface impedance becomes poorly matched to air characteristic impedance with temperature, thus leading to a decrease in sound absorption performance.

As shown in Figure **4b**, **c** and **d**, the comparisons between theoretical predictions and numerical simulations of three PPMs show good agreements at low frequencies (below 1000 Hz), whereas at high frequencies, the two still show a similar trend despite a slight difference. Previous studies showed that this phenomenon can be attributed to the different frequency ranges in which the pressure diffusion effect dominates in theory and simulation [30, 31]. The sound pressure diffusion effect is the entry of sound waves from macroscopic perforations into porous materials under sound pressure gradients. In numerical simulations, the pressure diffusion effect occurs mainly at low frequencies but becomes weak at high frequencies. The numerically simulated result is close to the actual sound propagation. However, in theoretical models, the pressure diffusion effect is considered in the whole frequency range, resulting in a slight difference between theoretical predictions and reality. As a result, the theoretical and simulated results

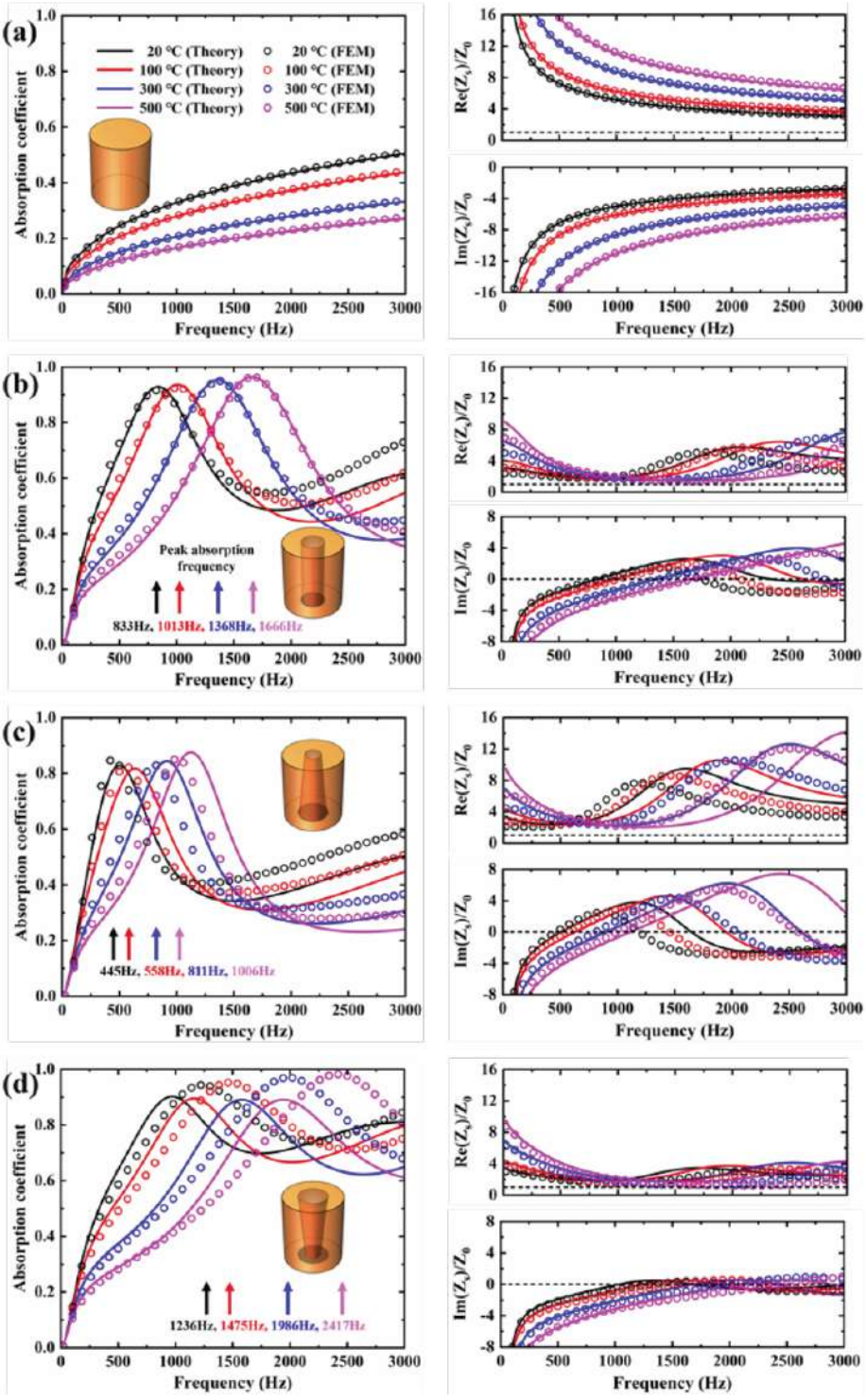

Figure 4: The comparison results between theoretical predictions and numerical simulations of sound absorption coefficient and normalized surface impedance.

are slightly different at high frequencies. However, this difference decreases with increasing temperature. This is because high temperatures promote the pressure diffusion effect at high frequencies in numerical simulations, thus reducing the high-frequency discrepancy between theory and simulation.

In addition, compared to non-perforated PMM, the sound absorption coefficient curves of PPMs exhibit a sound absorption peak. This is because the proper impedance matching produces an optimum sound absorption. According to Eq. 21, when the real part of surface impedance approaches 1 and the imaginary

part approaches 0, the absorption coefficients exhibit a peak value. With increasing temperature, these sound absorption peaks shift to the right, i.e., the peak frequency increases. This is because that high temperature raises the real part away from 1 and lowers the imaginary part away from 0 at the same frequency, thus delaying the occurrence of peaks. In short, the introduction of macroscopic perforations neutralizes the increased real part and the decreased imaginary part of surface impedance.

To visualize the sound pressure distributions, Figure **5** shows the sound pressure distributions of four porous materials at different temperatures and frequencies, where the dot-framed sub-figures are the sound pressure at peak frequency. At low frequencies, Figure **5a** shows the sound pressure is concentrated at the top of PMM, but Figure **5b**, **c** and **d** shows the sound pressure is concentrated at the bottom of PPMs. This is because low-frequency sound waves with larger wavelengths cannot fully enter the micropores of porous materials, but can reach the bottom via macroscopic perforations. As a result, a pressure gradient is created between macroscopic perforations and porous material, allowing sound pressures to penetrate from perforations into porous materials, resulting in a pressure diffusion effect. However, at high frequencies, sound waves with shorter wavelengths can enter the PMM with ease, resulting in a reduction of sound pressure at upper surfaces. Moreover, the sound pressure accumulated at the bottom of macroscopic perorations of three PPMs is gradually absorbed as frequency increases.

To further illustrate sound absorption mechanisms, Figure **6** shows that the sound energy dissipation density and sound intensity flow at these temperatures and frequencies, where the dot-framed sub-figures are those of peak frequency. Combining Figures **5** and **6** shows that the regions of high energy dissipation density and sound intensity flow coincide with the regions of high sound pressure. The principle of sound absorption is achieved by dissipating sound waves through the viscosity and thermal conduction in porous materials. For the PMMs, low-frequency sound waves with larger wavelengths cannot fully penetrate,

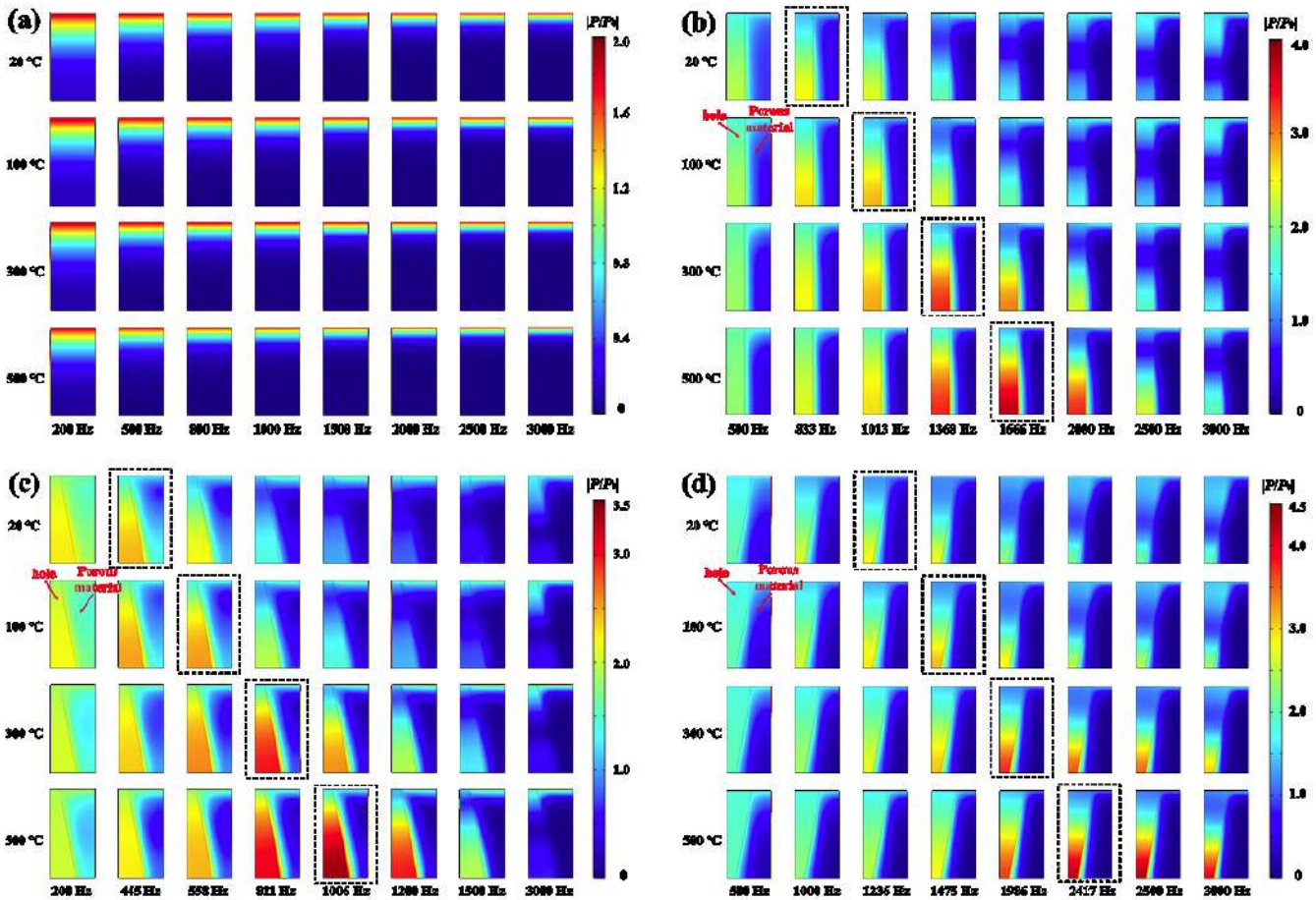

Figure 5: Sound pressure distributions normalized by the incident sound pressure P_0 at different temperatures.

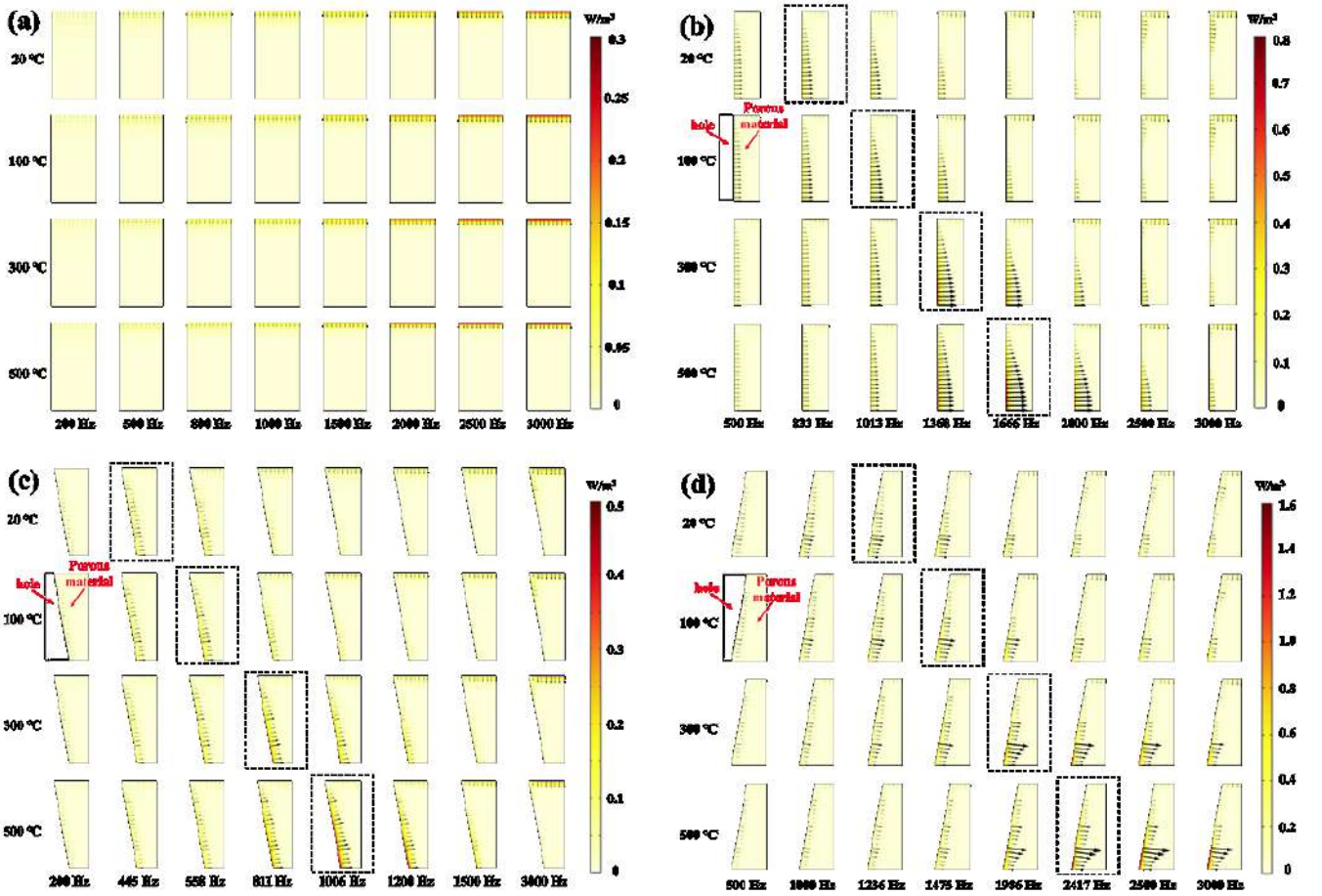

Figure 6: Sound energy dissipation density distributions (Color) and sound intensity flow distributions (Arrow) of porous materials at different temperatures.

resulting in less sound energy dissipation. As the frequency increases, sound waves enter porous material more easily, resulting in a significant increase in energy dissipation, mainly at the top of porous material. For the three PPMs, low-frequency sound waves at the bottom of perforations can enter porous materials more easily and be absorbed under the sound pressure diffusion effect. Therefore, sound energy dissipation mainly occurs at the sides of perforations and is stronger than that of PMM. As frequency increases, sound waves can also enter from the top of PPMs, further increasing sound energy dissipation.

Furthermore, Figure **7** shows the sound energy dissipation density of three PPMs at different temperatures. Obviously, the frequencies of energy dissipation density peaks are exactly the same as those in Figures **5** and **6**. The comparison shows that the frequencies of energy dissipation density peaks of three PPMs at the same temperature: $f_{NC\text{-}PPM} < f_{C\text{-}PPM} < f_{RC\text{-}PPM}$. Sound energy dissipation density is correlated with sound absorption. Sound absorption peaks occur at the frequency of energy dissipation density peaks. As the temperature rises, sound energy dissipation density peaks shift to the right, and sound absorption peaks also shift to the right. The sound energy dissipation density at peak frequency and its adjacent frequencies increases with temperature, indicating that the sound absorption in this frequency range is enhanced.

4. RESULTS AND DISCUSSION

4.1. Influence of Perforation Shapes

To explore the influence of perforation shapes on sound absorption, Figure **8** shows the absorption coefficients of PPMs with the same perforated volume but with different perforated shapes at different temperatures. Obviously, the three PPMs exhibit much better sound absorption than the PMM, especially at low and mid frequencies, and this advantage is further extended at high temperatures. This is because the pressure diffusion effect of PPMs enhances sound absorption, and high temperature enhances the

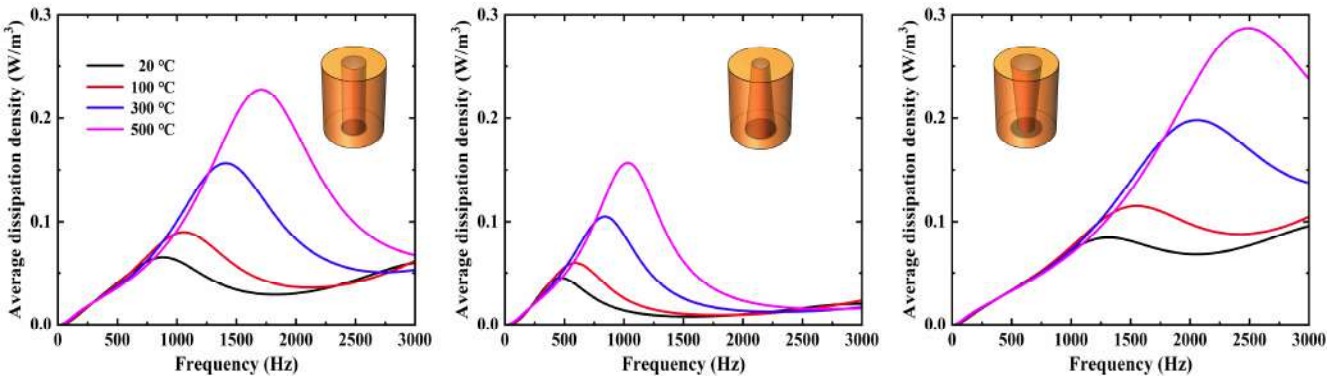

Figure 7: Sound energy dissipation density of PPMs at different temperatures.

pressure diffusion effect, making the sound absorption even stronger. Therefore, the low and mid-frequency sound absorption of porous materials can be improved by constructing macroscopic perforations on them. Furthermore, the absorption coefficient curves of three PPMs exhibit sound absorption peaks, whose peak frequencies satisfy: $f_{(NC\text{-}PPM)} < f_{(C\text{-}PPM)} < f_{(RC\text{-}PPM)}$, and these peak frequencies increase with temperature, i.e., the peak shifts to the right. This suggests that the PPMs with different perforated shapes have their own frequency ranges for optimal sound absorption. Therefore, at a given frequency and temperature, choosing an appropriate perforation shape greatly benefit sound absorption.

4.2. Influence of Cylindrical Perforation Sizes

To explore the influence of cylindrical perforation sizes on sound absorption, Figure **9** shows the sound absorption coefficient curves of the C-PPMs with different hole radii at different temperatures. As the hole radius increases, the sound absorption coefficients increase significantly and present a peak value. The sound absorption peaks increase and then decrease and shift to the right with hole radius. This is

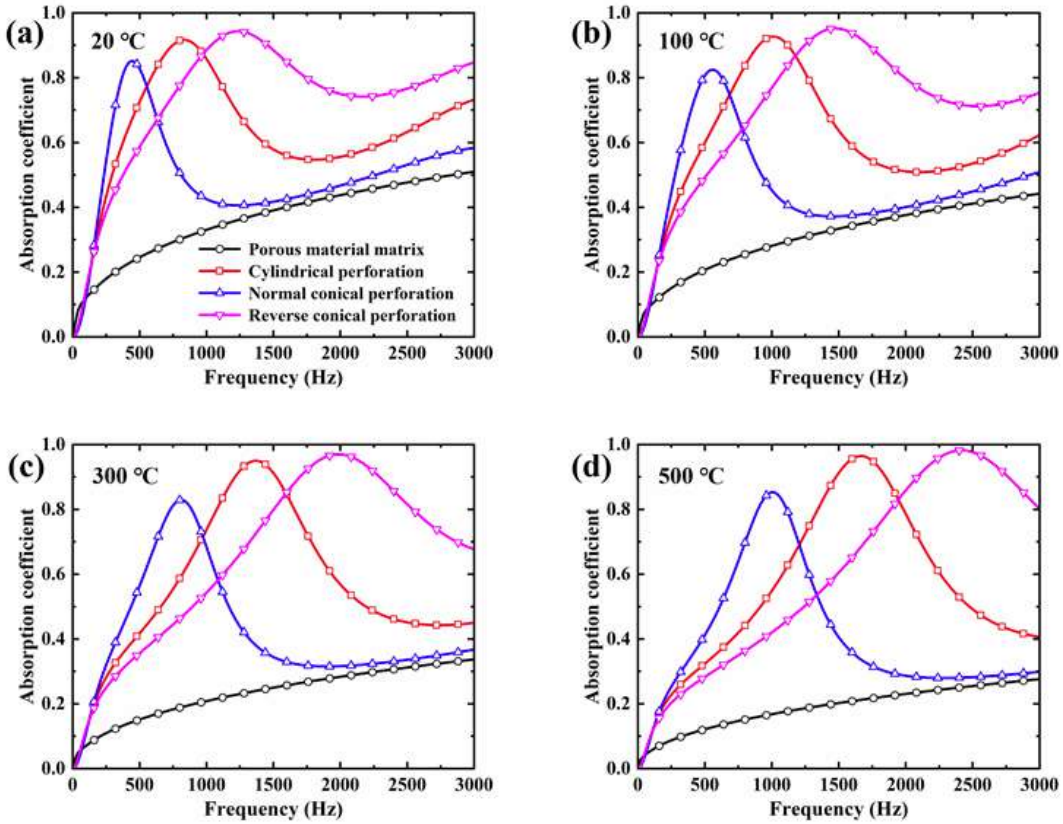

Figure 8: The comparisons of the sound absorption coefficients of the PPMs with different shaped perforations at different temperatures.

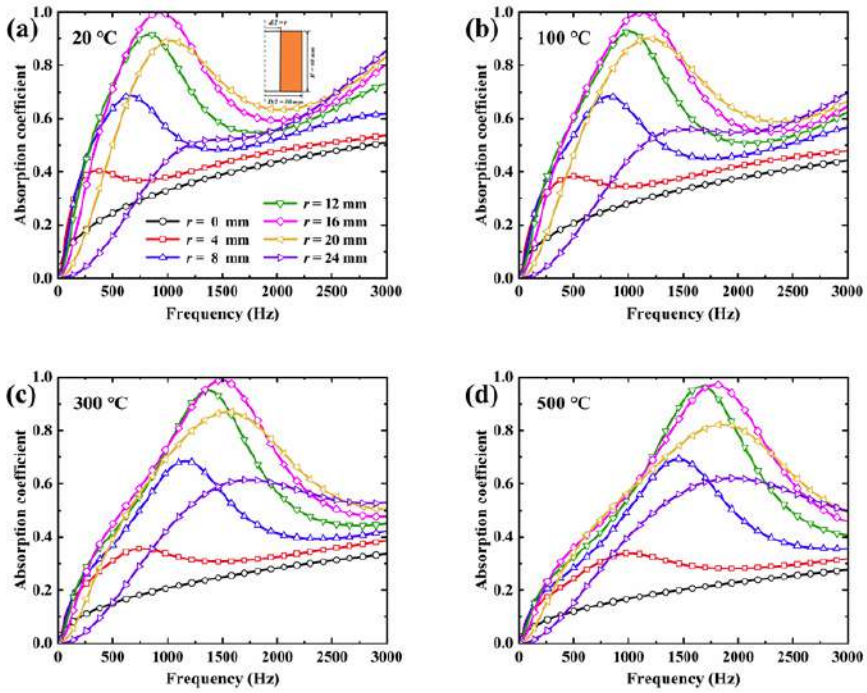

Figure 9: The comparisons of the sound absorption coefficients of the PPMs with different hole diameters at different temperatures.

because sound waves cannot fully enter the porous materials when perforated hole is too small, while the volume of porous materials is reduced when perforated hole is too large, both of which lead to a decrease in sound absorption.

Moreover, Figure **10** shows the sound absorption coefficients of the C-PPMs with different perforation depths at different temperatures. As the hole depth increases, the sound absorption coefficients increase significantly and present a peak value. The sound

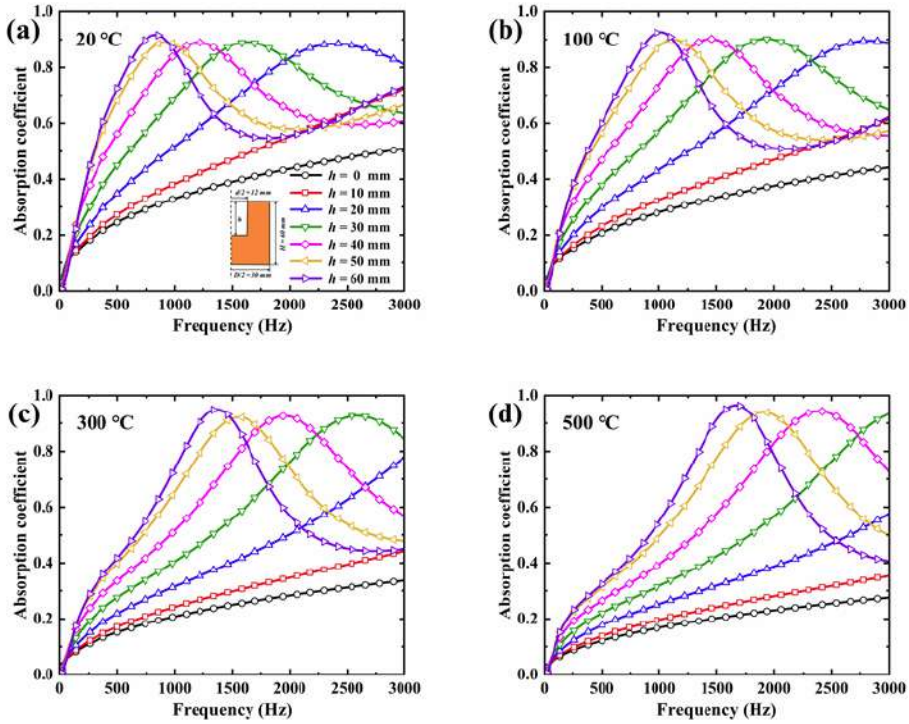

Figure 10: The comparisons of the sound absorption coefficients of the PPMs with different hole depths at different temperatures.

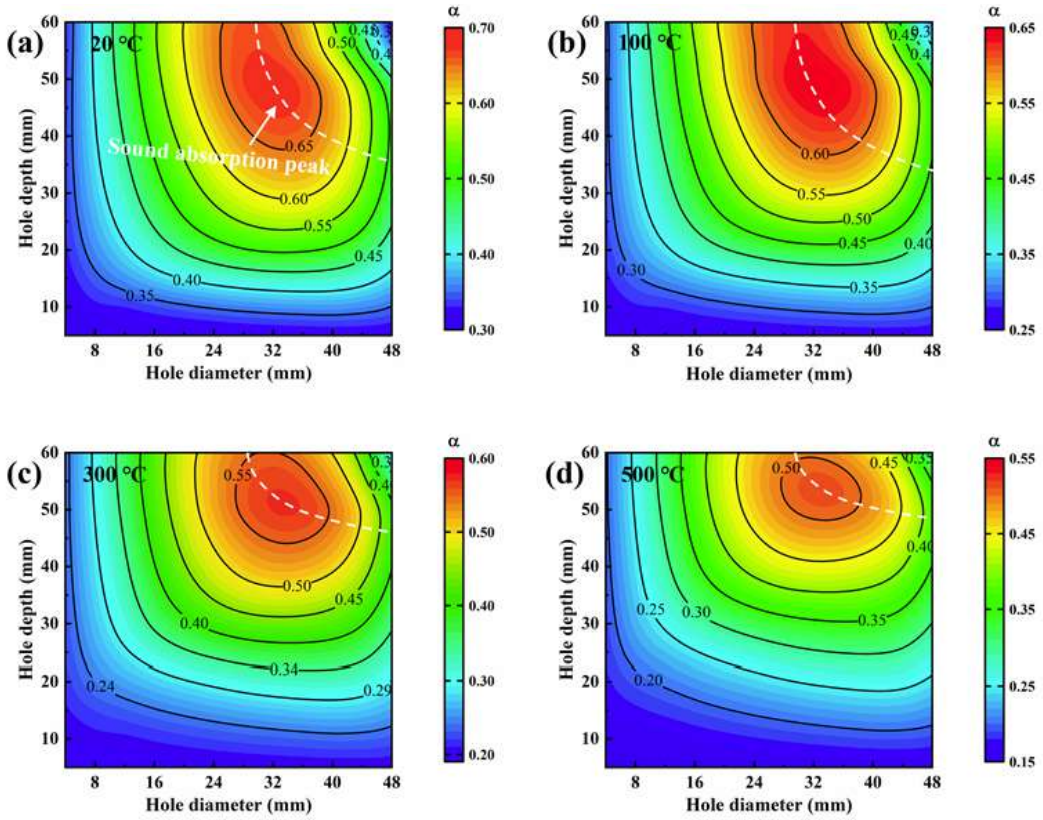

Figure 11: Distributions of α_{SAA} over the 12-octave frequencies of C-PPM at different temperatures.

absorption peaks shift to the left with hole depth. This suggests that the C-PPMs with different hole depths have different optimal sound absorption frequency ranges, and that increasing hole depth can improve low-frequency sound absorption, especially at high temperatures.

More importantly, the sound absorption of C-PPMs can be optimized based on the above perforation sizes. By finding the optimum hole diameter and depth, the overall sound absorption can be significantly improved. A widely used method of assessing the overall sound absorption is the Sound Absorption Average (α_{SAA}) [43], which uses an average sound absorption coefficient from twelve 1/3 octave frequencies. Figure **11** shows that the SAA distributions of 12-octave frequencies (200, 250, 315, 400, 500, 630, 800, 1000, 1250, 1600, 2000, 2500 Hz) at different temperatures, where the dashed lines illustrate the optimum combination of hole diameter and depth for the best sound absorption. Surprisingly, at all temperatures, the optimal sound absorption was always located roughly in the region of hole diameter d = 32 mm and hole depth h = 50 mm. The SAA mapping depicts the optimum hole sizes for an overall assessment of sound absorption in the whole frequency range.

4.3. Influence of Conical Perforation Gradients

To explore the influence of conical perforation gradients on sound absorption, Figure **12** shows the sound absorption coefficient curves of the NC-PPM with the same perforation volume but with different perforation gradients. Obviously, the influence of perforation gradients mainly occurs at low and mid frequencies. Increasing the perforation angle θ of NC-PPM can improve low-frequency sound absorption. As the perforation angle θ increases, the sound absorption peaks shift to the left and decrease slightly, especially at high temperatures.

Moreover, Figure **13** shows the absorption coefficient curves of the RC-PPM with the same perforation volume but with different perforation gradients. Obviously, the influence of perforation gradients mainly occurs at mid and high frequencies. Increasing the perforation angle θ of RC-PPM can improve high-frequency sound absorption. As the perforation angle θ increases, the sound absorption peaks shift to the right, especially at high temperatures.

4.4. Influence of Material Properties

The acoustic parameters of sound-absorbing materials have an important impact on sound

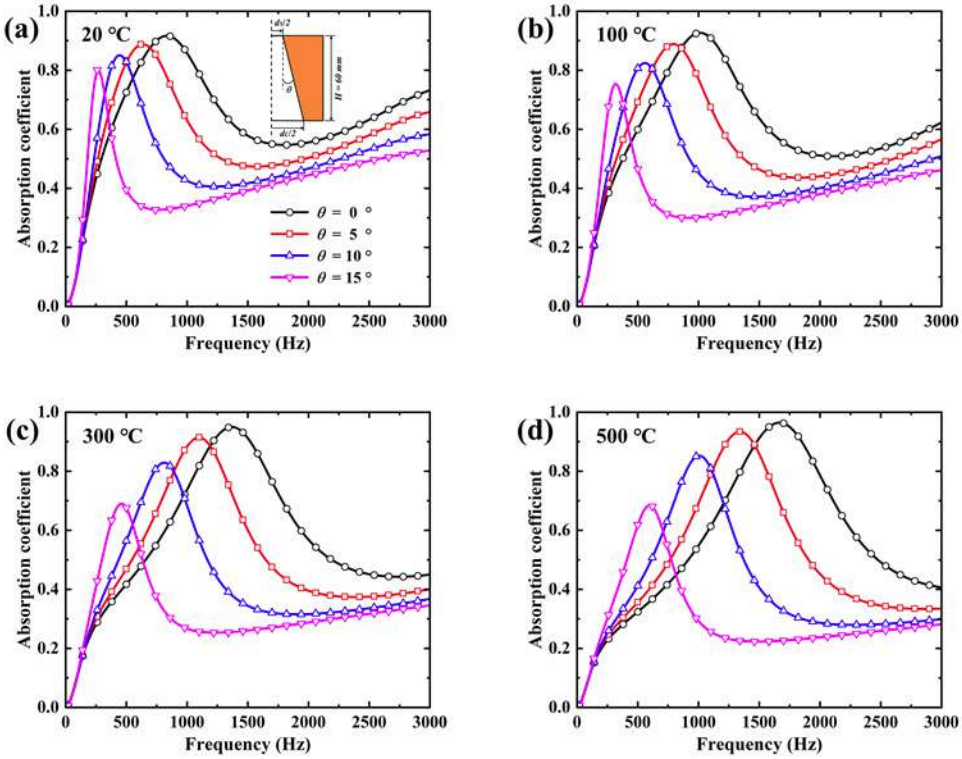

Figure 12: Sound absorption of the NC-PPMs with different perforation gradients at different temperatures.

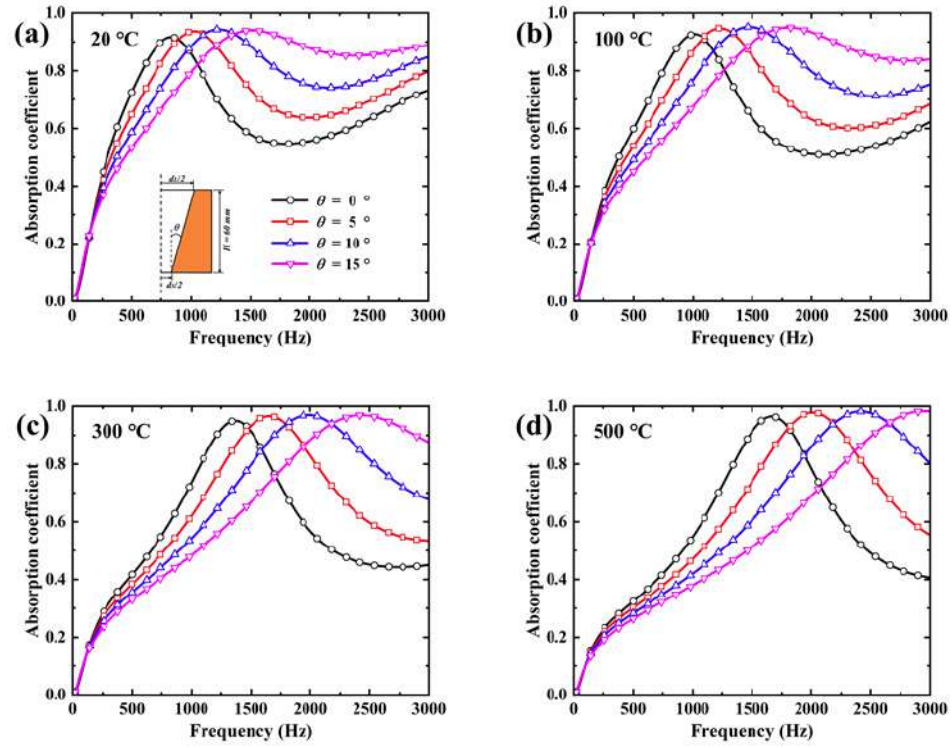

Figure 13: Sound absorption of the RC-PPMs with different perforation gradients at different temperatures.

absorption, especially the static flow resistivity σ_m [38]. This is because the static flow resistivity is related to the surface impedance of porous materials. To explore the influence of material properties and also to discover acoustic materials with better sound absorption, we comparatively studied the sound absorption of six

Table 2: The Acoustic Parameters of Different Porous Materials at 20 ℃ [29, 38]

Materials	σ_m [N·s/m^4]	ϕ_m	$\alpha_{\infty m}$	Λ_m [μm]	Λ_m' [μm]
Mat-1	50000	0.97	1.070	175.0	175.0
Mat-2	75094	0.90	1.085	56.3	90.0
Mat-3	135000	0.94	2.100	49.0	166
Mat-4	190090	0.85	1.127	36.2	56.6
Mat-5	305767	0.89	3.700	21.6	53.6
Mat-6	489336	0.90	1.050	19.7	36.0

porous material matrixes. Their acoustic parameters are shown in Table **2**.

The sound absorption of six materials with the same geometric parameters is compared. Figure **14** shows the sound absorption coefficient and normalized surface impedance at different temperatures. From Mat-1 to Mat-6, as the static flow resistivity σ_m increases, the sound absorption coefficient decreases. This can be explained by the relationship between static flow resistivity and surface impedance. The lower the static flow resistivity, the smaller and closer to 1 the real part of surface impedance, and the larger and closer to 0 the imaginary part. This implies a better match with air impedance, which results in better sound absorption. Conversely, the higher the static flow resistivity, the larger and further away from 1 the real part of surface impedance, and the smaller and further away from 0 the imaginary part. This implies a poor match with air impedance, which results in poor sound absorption.

In addition, as the temperature rises, the sound absorption coefficients of the six materials decrease. This is because the real part of surface impedance increases and moves away from 1 as the temperature increases, while the imaginary part decreases and moves away from 0. Again, this can be attributed to the change in static flow resistivity caused by high temperature. According to Eq. 45, the static flow resistivity σ_m increases with increasing temperature. Based on the above analysis, an increase in static flow resistivity leads to the real part of surface impedance increasing and moving away from 1, and the imaginary part decreasing and moving away from 0, which ultimately leads to a decrease in sound absorption.

5. CONCLUSIONS

In this paper, high-temperature sound absorption characteristics of PMM and three PPMs are comparatively studied theoretically and numerically. The temperature effect is studied by analyzing the sound absorption coefficients and surface impedances.

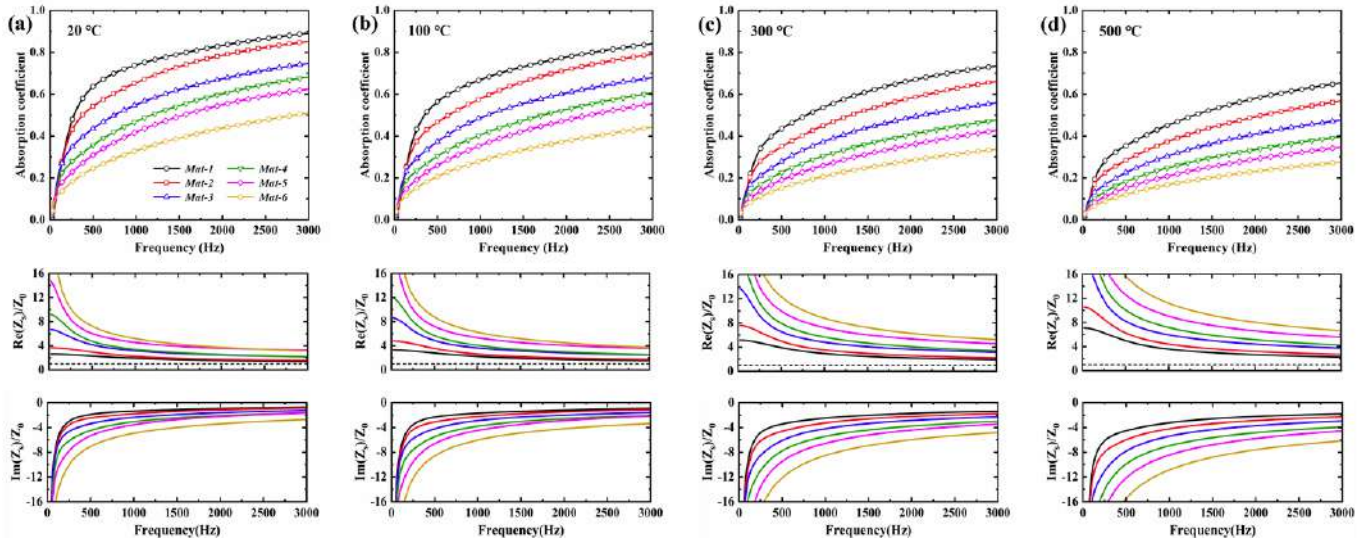

Figure 14: Sound absorption coefficient and normalized surface impedance of different sound-absorbing material matrixes at different temperatures.

The results show that the PPMs have better sound absorption than the PPM, especially at low frequencies. This is attributed to the pressure diffusion effect of PPMs, and high temperatures enhance this effect over a wider frequency range. The sound absorption mechanism is revealed from the numerical distribution of sound pressure, sound energy dissipation density and sound intensity flow. Furthermore, the three PPMs have sound absorption peaks in different frequency ranges, which are in the following order: $f_{(NC\text{-}PPM)} < f_{(C\text{-}PPM)} < f_{(RC\text{-}PPM)}$. Because high temperatures prevent sound waves from entering porous material, it delays the appearance of peaks and moves it to a higher frequency. Finally, the influence of perforation shapes, sizes and material properties on sound absorption were discussed. The three PPMs, NC-PPM, C-PPM and RC-PPM exhibit good sound absorption in low-frequency, mid-frequency and high-frequency ranges, respectively. The proper combination of cylindrical perforation diameter and depth of C-PPM helps to improve the overall sound absorption. Increasing the conical angle of NC-PPM improves low-frequency sound absorption, while increasing the conical angle of RC-PPM improves high-frequency sound absorption. The static flow resistivity of materials has an impact on sound absorption, with small static flow resistivity having good sound absorption. This paper can guide the design, optimization and application of good PPMs to improve their high-temperature sound absorption.

DATA AVAILABILITY STATEMENT

The data that support this study are available from the corresponding author upon reasonable request.

CONFLICTS OF INTEREST

The authors declare no conflict of interest.

REFERENCES

D. Zhao, X. Li, A review of acoustic dampers applied to combustion chambers in aerospace industry, Progress in Aerospace Sciences, 74 (2015) 114-130. https://doi.org/10.1016/j.paerosci.2014.12.003

L. Cao, Q. Fu, Y. Si, B. Ding, J. Yu, Porous materials for sound absorption, Composites Communications, 10 (2018) 25-35. https://doi.org/10.1016/j.coco.2018.05.001

F. Sun, H. Chen, J. Wu, K. Feng, Sound absorbing characteristics of fibrous metal materials at high temperatures, Applied Acoustics, 71 (2010) 221-235. https://doi.org/10.1016/j.apacoust.2009.09.001

J. Hui Wu, Z.P. Hu, H. Zhou, Sound absorbing property of porous metal materials with high temperature and high sound pressure by turbulence analogy, Journal of Applied Physics, 113 (2013). https://doi.org/10.1063/1.4804951

S. Ren, F. Xin, T.J. Lu, C. Zhang, A semi-analytical model for the influence of temperature on sound propagation in sintered metal fiber materials, Materials & Design, 134 (2017) 513-522. https://doi.org/10.1016/j.matdes.2017.09.007

M.J. Cops, J.G. McDaniel, E.A. Magliula, D.J. Bamford, J. Bliefnick, Measurement and analysis of sound absorption by a composite foam, Applied Acoustics, 160 (2020) 107138. https://doi.org/10.1016/j.apacoust.2019.107138

D. Cuiyun, C. Guang, X. Xinbang, L. Peisheng, Sound absorption characteristics of a high-temperature sintering porous ceramic material, Applied Acoustics, 73 (2012) 865-871. https://doi.org/10.1016/j.apacoust.2012.01.004

X. Dong, Q. An, S. Zhang, H. Yu, M. Wang, Porous ceramics based on high-thermal-stability Al2O3–ZrO2 nanofibers for thermal insulation and sound absorption applications, Ceramics International, 49 (2023) 31035-31045. https://doi.org/10.1016/j.ceramint.2023.07.048

J. Chen, P. Liu, J. Sun, Sound absorption performance of a lightweight ceramic foam, Ceramics International, 46 (2020) 22699-22708. https://doi.org/10.1016/j.ceramint.2020.06.033

M. Carlesso, R. Giacomelli, S. Günther, D. Koch, S. Kroll, S. Odenbach, K. Rezwan, Near-net-shaped porous ceramics for potential sound absorption applications at high temperatures, Journal of the American Ceramic Society, 96 (2013) 710-718. https://doi.org/10.1111/jace.12160

Z. Li, Z. Wang, Z. Guo, X. Wang, X. Liang, Ultra-broadband sound absorption of a hierarchical acoustic metamaterial at high temperatures, Applied Physics Letters, 118 (2021). https://doi.org/10.1063/5.0044656

Z. Guo, Z. Li, K. Zeng, X. Lu, J. Ye, Z. Wang, Hierarchical-porous acoustic metamaterials: A synergic approach to enhance broadband sound absorption, Materials & Design, 241 (2024) 112943. https://doi.org/10.1016/j.matdes.2024.112943

X. Wang, R. Qin, J. Lu, M. Huang, X. Zhang, B. Chen, Laser additive manufacturing of hierarchical multifunctional chiral metamaterial with distinguished damage-resistance and low-frequency broadband sound-absorption capabilities, Materials & Design, 238 (2024) 112659. https://doi.org/10.1016/j.matdes.2024.112659

M. Yang, Z. Chen, L. Yang, Y. Ding, X. Chen, M. Li, Q. Wu, T. Liu, Hierarchically porous networks structure based on flexible SiO2 nanofibrous aerogel with excellent low frequency noise absorption, Ceramics International, 49 (2023) 301-308. https://doi.org/10.1016/j.ceramint.2022.08.344

C. Dong, Z. Liu, R. Pierce, X. Liu, X. Yi, Sound absorption performance of a micro perforated sandwich panel with honeycomb-hierarchical pore structure core, Applied Acoustics, 203 (2023) 109200. https://doi.org/10.1016/j.apacoust.2022.109200

L. Shen, H. Zhang, Y. Lei, Y. Chen, M. Liang, H. Zou, Hierarchical pore structure based on cellulose nanofiber/melamine composite foam with enhanced sound absorption performance, Carbohydrate Polymers, 255 (2021) 117405. https://doi.org/10.1016/j.carbpol.2020.117405

Z. Mei, Y. Lyu, X. Li, X. Cheng, J. Yang, Parallel-coupled hierarchical and reconfigurable structure for broadband sound absorption, Applied Acoustics, 221 (2024) 109990. https://doi.org/10.1016/j.apacoust.2024.109990

Y. Tang, F. Xin, T.J. Lu, Sound absorption of micro-perforated sandwich panel with honeycomb-corrugation hybrid core at high temperatures, Composite Structures, 226 (2019) 111285. https://doi.org/10.1016/j.compstruct.2019.111285

P. Zhang, Z. Li, B. Liu, Y. Zhou, M. Zhao, G. Sun, S. Pei, X. Kong, P. Bai, Sound absorption performance of micro-perforated plate

sandwich structure based on triply periodic minimal surface, Journal of Materials Research and Technology, 27 (2023) 386-400. https://doi.org/10.1016/j.jmrt.2023.09.237

Z. Li, Y. Zhou, X. Kong, P. Zhang, S. Pei, L. Ge, Y. Nie, B. Liu, Sound absorption performance of a micro-perforated plate sandwich structure based on selective laser melting, Virtual and Physical Prototyping, 19 (2024) e2321607. https://doi.org/10.1080/17452759.2024.2321607

J. Huang, J. Wang, T. Ma, H. Wei, S. Zhang, G. Wang, L. Wang, Q. Wang, W. Zhou, Z. Zhang, Composite structure with porous material and parallel resonators for broadband sound absorption at low-to-mid frequencies, Applied Acoustics, 225 (2024) 110193. https://doi.org/10.1016/j.apacoust.2024.110193

D. Wang, Y. Xiao, S. Wang, Z. Huang, J. Wen, Ultra-broadband sound-absorbing metastructure with Helmholtz resonator and porous material modulation crown, Materials & Design, 246 (2024) 113351. https://doi.org/10.1016/j.matdes.2024.113351

J.-P. Groby, C. Lagarrigue, B. Brouard, O. Dazel, V. Tournat, B. Nennig, Enhancing the absorption properties of acoustic porous plates by periodically embedding Helmholtz resonators, The Journal of the Acoustical Society of America, 137 (2015) 273-280. https://doi.org/10.1121/1.4904534

Y. Li, Y. Lin, S. Yao, C. Shi, Low-frequency broadband sound absorption of the metastructure with extended tube resonators and porous materials, Applied Acoustics, 217 (2024) 109827. https://doi.org/10.1016/j.apacoust.2023.109827

X.-F. Zhu, S.-K. Lau, Z. Lu, W. Jeon, Broadband low-frequency sound absorption by periodic metamaterial resonators embedded in a porous layer, Journal of Sound and Vibration, 461 (2019) 114922. https://doi.org/10.1016/j.jsv.2019.114922

G. Jin, K. Shi, T. Ye, J. Zhou, Y. Yin, Sound absorption behaviors of metamaterials with periodic multi-resonator and voids in water, Applied Acoustics, 166 (2020) 107351. https://doi.org/10.1016/j.apacoust.2020.107351

H. Zhang, Y. Wang, H. Zhao, K. Lu, D. Yu, J. Wen, Accelerated topological design of metaporous materials of broadband sound absorption performance by generative adversarial networks, Materials & Design, 207 (2021) 109855. https://doi.org/10.1016/j.matdes.2021.109855

Z. Xiao, P. Gao, D. Wang, X. He, Y. Qu, L. Wu, Accelerated design of low-frequency broadband sound absorber with deep learning approach, Mechanical Systems and Signal Processing, 211 (2024) 111228. https://doi.org/10.1016/j.ymssp.2024.111228

X. Liu, F. Xin, C. Zhang, High-temperature effect on the sound absorption of cylindrically perforated porous materials, Journal of Applied Physics, 130 (2021). https://doi.org/10.1063/5.0050217

W. Zhang, X. Liu, F. Xin, Sound absorption performance of helically perforated porous metamaterials at high temperature, Materials & Design, 225 (2023) 111437. https://doi.org/10.1016/j.matdes.2022.111437

W. Zhang, X. Liu, F. Xin, Normal incidence sound absorption of an acoustic labyrinthine metal-fibers-based porous metamaterial at high temperature, International Journal of Mechanical Sciences, 237 (2023) 107821. https://doi.org/10.1016/j.ijmecsci.2022.107821

X. Olny, C. Boutin, Acoustic wave propagation in double porosity media, The Journal of the Acoustical Society of America, 114 (2003) 73-89. https://doi.org/10.1121/1.1534607

D.L. Johnson, J. Koplik, R. Dashen, Theory of dynamic permeability and tortuosity in fluid-saturated porous media, Journal of fluid mechanics, 176 (1987) 379-402. https://doi.org/10.1017/S0022112087000727

Y. Champoux, J.F. Allard, Dynamic tortuosity and bulk modulus in air-saturated porous media, Journal of applied physics, 70 (1991) 1975-1979. https://doi.org/10.1063/1.349482

F.C. Sgard, X. Olny, N. Atalla, F. Castel, On the use of perforations to improve the sound absorption of porous materials, Applied acoustics, 66 (2005) 625-651. https://doi.org/10.1016/j.apacoust.2004.09.008

X. Liu, X. Ma, C. Yu, F. Xin, Sound absorption of porous materials perforated with holes having gradually varying radii, Aerospace Science and Technology, 120 (2022) 107229. https://doi.org/10.1016/j.ast.2021.107229

X. Liu, C. Yu, F. Xin, Gradually perforated porous materials backed with Helmholtz resonant cavity for broadband low-frequency sound absorption, Composite Structures, 263 (2021) 113647. https://doi.org/10.1016/j.compstruct.2021.113647

X. Liu, M. Liu, F. Xin, Sound absorption of a perforated panel backed with perforated porous material: Energy dissipation of Helmholtz resonator cavity, Mechanical Systems and Signal Processing, 185 (2023) 109762. https://doi.org/10.1016/j.ymssp.2022.109762

D. Lee, Y. Kwon, Estimation of the absorption performance of multiple layer perforated panel systems by transfer matrix method, Journal of sound and vibration, 278 (2004) 847-860. https://doi.org/10.1016/j.jsv.2003.10.017

W. Xu, D. Yu, J. Wen, Simple meta-structure that can achieve the quasi-perfect absorption throughout a frequency range of 200–500 Hz at 350° C, Applied Physics Express, 13 (2020) 047001. https://doi.org/10.35848/1882-0786/ab7bc7

D. Christie, Measurement of the acoustic properties of a sound absorbing material at high temperatures, Journal of Sound and Vibration, 46 (1976) 347-355. https://doi.org/10.1016/0022-460X(76)90859-2

Q. Liu, X. Liu, C. Zhang, F. Xin, High-temperature and low-frequency acoustic energy absorption by a novel porous metamaterial structure, Acta Mechanica Solida Sinica, 34 (2021) 872-883. https://doi.org/10.1007/s10338-021-00253-9

X. Cai, J. Yang, G. Hu, T. Lu, Sound absorption by acoustic microlattice with optimized pore configuration, The Journal of the Acoustical Society of America, 144 (2018) EL138-EL143. https://doi.org/10.1121/1.5051526

Received on 14-09-2025 Accepted on 24-10-2025 Published on 05-11-2025